

Crystal growth, structure and crystal field splitting and fitting of Yb:$GdScO_3$

Jia-Hong Li(李加红), Qing-Li Zhang(张庆礼), Gui-Hua Sun(孙贵花), Jin-Yun Gao(高进云), Ren-Qin Dou(窦仁勤), Xiao-Fei Wang(王小飞), and Shou-Jun Ding(丁守军)

Citation Chin. Phys. B, 2024, 33 (**11**): 117601. DOI: 10.1088/1674-1056/ad72d3
Journal homepage: http://cpb.iphy.ac.cn; http://iopscience.iop.org/cpb

What follows is a list of articles you may be interested in

Low-temperature ferromagnetism in tensile-strained $LaCoO_{2.5}$ thin film

Yang-Yang Fan(范洋洋), Jing Wang(王晶), Feng-Xia Hu(胡凤霞), Bao-He Li(李宝河), Ai-Cong Geng(耿爱丛), Zhuo Yin(殷卓), Cheng Zhang(张丞), Hou-Bo Zhou(周厚博), Meng-Qin Wang(王梦琴), Zi-Bing Yu(尉紫冰), and Bao-Gen Shen(沈保根)

Chin. Phys. B, 2023, 32 (**8**): 087504. DOI: 10.1088/1674-1056/acafdc

Determination of charge-compensated C_{3v} (II) centers for Er^{3+} ions in CdF_2 and CaF_2 crystals

Rui-Peng Chai(柴瑞鹏), Dan-Hui Hao(郝丹辉), Dang-Li Gao(高当丽), and Qing Pang(庞庆)

Chin. Phys. B, 2021, 30 (**3**): 037601. DOI: 10.1088/1674-1056/abc3b0

Magnetic properties of the double perovskite compound Sr_2YRuO_6

N. EL Mekkaoui, S. Idrissi, S. Mtougui, I. EL Housni, R. Khalladi, S. Ziti, H. Labrim, L. Bahmad

Chin. Phys. B, 2019, 28 (**9**): 097503. DOI: 10.1088/1674-1056/ab3441

Covalent bonding and *J-J* mixing effects on the EPR parameters of Er^{3+} ions in GaN crystal

Rui-Peng Chai(柴瑞鹏), Long Li(李隆), Liang Liang(梁良), Qing Pang(庞庆)

Chin. Phys. B, 2016, 25 (**7**): 077601. DOI: 10.1088/1674-1056/25/7/077601

High-energy pulse generation using Yb-doped Q-switched fiber laser based on single-walled carbon nanotubes

Wang Jun-Li (王军利), Wang Xue-Ling (汪雪玲), He Bo-Rong (贺博荣), Zhu Jiang-Feng (朱江峰), Wei Zhi-Yi (魏志义), Wang Yong-Gang (王勇刚)

Chin. Phys. B, 2015, 24 (**9**): 097601. DOI: 10.1088/1674-1056/24/9/097601

Crystal growth, structure and crystal field splitting and fitting of Yb:$GdScO_3$

Jia-Hong Li(李加红)[1,2,3], Qing-Li Zhang(张庆礼)[1,3,†], Gui-Hua Sun(孙贵花)[1,3,‡], Jin-Yun Gao(高进云)[1,3], Ren-Qin Dou(窦仁勤)[1,3], Xiao-Fei Wang(王小飞)[1,3], and Shou-Jun Ding(丁守军)[1,3,4]

[1] *Key Laboratory of Photonic Devices and Materials of Anhui Province, Anhui Institute of Optics and Fine Mechanics, Hefei Institutes of Physical Science, Chinese Academy of Sciences, Hefei* 230031, *China*
[2] *University of Science and Technology of China, Hefei* 230026, *China*
[3] *Advanced Laser Technology Laboratory of Anhui Province, Hefei* 230026, *China*
[4] *School of Science and Engineering of Mathematics and Physics, Anhui University of Technology, Maanshan* 243002, *China*

(Received 17 June 2024; revised manuscript received 22 August 2024; accepted manuscript online 23 August 2024)

A good quality (5 at.% Yb:$GdScO_3$) single crystal of Φ30 mm × 37 mm was grown successfully by the Czochralski method. Its structure is studied by the x-ray diffraction (XRD), and its atomic coordinates are obtained by Rietveld refinement. The crystal field energy level splitting of Yb^{3+} in $GdScO_3$ is determined by employing the absorption and photoluminescence spectra at 8 K. Only $^2F_{7/2}(4)$ is far from the ground state $^2F_{7/2}(1)$ by 710 cm^{-1} among the crystal field energy levels split from $^2F_{7/2}$, so it is more easier to realize the laser operation of $^2F_{5/2}(1)\rightarrow{}^2F_{7/2}(4)$ with wavelength 1060 nm. The spin–orbit coupling parameters and intrinsic crystal field parameters (CFPs). The intrinsic crystal field parameters $\bar{B}_k$ ($k = 2, 4, 6$) of the crystal were fitted by the superposition model. The CFPs evaluated with $\bar{B}_k$ and coordination factor are taken as the initial parameters to fit the crystal field energy levels of the crystal, and the crystal field parameters B_q^k are obtained finally with the root-mean-square deviation 9 cm^{-1}. It is suggested that the ligand point charge, covalency and overlap interaction are slightly weaker than charge interpenetration and coulomb exchange interaction for Yb^{3+} in $GdScO_3$. The obtained Hamiltonian parameters can be used to calculate crystal field energy levels and wave functions of Yb:$GdScO_3$ to analyze the mechanism of the luminescence or laser.

Keywords: rare earth scandate, crystal field, photoluminescence, laser crystal

PACS: 76.30.Kg, 75.10.Dg, 78.55.–m, 42.55.Tv **DOI:** 10.1088/1674-1056/ad72d3

1. Introduction

Rare-earth scandate crystals ($REScO_3$, RE = rare earth ions) are promising candidates to replace SiO_2 in Si-based metal-oxide-semiconductor field effect transistors (MOSFETs) because of their high dielectric constants, high proton conductivity, large optical band gaps (> 5.5 eV) and good thermodynamic stability compared to silicon.[1–9] Rare earth scandium is ferroelastic, as opposed to $LaAlO_3$ or $BaTiO_3$ substrates, and growth of ferroelastic domains is a unique advantage of existing rare earth scandate substrates. It is mainly used in epitaxial growth of multiferroic, ferroelectric and superconducting perovskite materials. Understanding of functional ABO_3 perovskite-type oxides is an active research area with relevance to both fundamental and application-related issues.[10–17] A special aspect of perovskite is its ability to incorporate almost all elements in the periodic table into its structure, resulting in a large number of observed structural distortions, which in turn lead to an extraordinary abundance of physical properties in the perovskite family.[18]

Gadolinium scandate ($GdScO_3$) crystal is perovskite structure ($GdFeO_3$ type) and belongs to an orthorhombic system with space group of *Pnma* (No. 62). This crystal is a promising efficient laser host and can be grown by the conventional Czochralski method.[19–25] Firstly, $GdScO_3$ crystal has stable chemical properties, high thermal conductivity and excellent mechanical properties. Secondly, the site symmetry of Gd^{3+} is low, which is beneficial to removing the parity transition prohibition in 4f configuration of rare earth ions and improving the luminescence efficiency. Thirdly, the crystal has large birefringence effect. When pumped by a high power laser diode, its natural birefringence is much larger than thermal birefringence and dominant, which can eliminate the adverse effects caused by thermal birefringence such as thermal depolarization loss.[26] Lastly, the crystal has a lower phonon energy of 452 cm^{-1} in comparison with other oxide crystals, such as YAG (860 cm^{-1}), which is beneficial to reduce the probability of multi-phonon relaxation.[27–31]

Yb^{3+} has a typical f–f transition with good luminescence characteristics, which has ground multiple state $^2F_{7/2}$ and excited multiple state $^2F_{5/2}$ with the interval of about 10000 cm^{-1}.[32] It has no excited state absorption, upconversion and cross relaxation, resulting in the high efficiency and low thermal load during the laser operation.[33–40] In addition, its broad absorption band from f–f transition matches well

†Corresponding author. E-mail: zql@aiofm.ac.cn
‡Corresponding author. E-mail: ghsun@aiofm.ac.cn

© 2024 Chinese Physical Society and IOP Publishing Ltd

with the emission wavelength of 900–1000 nm of commercial InGaAs laser diodes (LDs), which make it possible to develop high power solid state laser.[41–44] It has been reported that Yb:$GdScO_3$ is a high-efficiency laser material and it achieved 13.45 W continuous laser output at 1063.9 nm.[45] However, its structure, crystal field splitting and Hamiltonian parameters have not been reported. In this work, 5 at.% Yb:$GdScO_3$ single crystal was grown by the Czochralski method and its structure is determined by Rietveld refinement to its x-ray diffraction (XRD). Crystal filed energy splitting of Yb^{3+} in $GdScO_3$ host is obtained with the photoluminescence and absorption spectra at the low temperature. In addition, Hamiltonian parameters of Yb^{3+} in the crystal is fitted, which can be used to investigate the luminescence mechanism such as optical transition probability.

2. Experiment

2.1. Crystal growth

In the experiment, 5 at.%Yb:$GdScO_3$ single crystal was grown by employing the Czochralski method with an Ir crucible in N_2 atmosphere. Raw materials are Sc_2O_3 (99.9995%), Gd_2O_3 (99.995%), and Yb_2O_3 (99.995%). The raw materials were weighted with the following stoichiometric ratio:

$$(1-x)Yb_2O_3 + xGd_2O_3 + Sc_2O_3 \rightarrow 2Yb_{(1-x)}Gd_xScO_3, \quad (1)$$

where $x = 0.05$. The raw materials were mixed thoroughly. In order to reduce the volume of the raw materials, the mixture was pressed into disks of about Φ55 mm × 20 mm, and calcined at 1250 ℃ in a box furnace for 24 h in atmosphere to form polycrystalline through solid state reaction. After calcination, the polycrystalline disks were taken out and loaded into an iridium crucible of Φ60 mm × 60 mm for crystal growth in a Czochralski furnace JGD80, made in the 26th Institute of CETC. After thermal insulators and single crystal seed with ⟨100⟩ orientation were installed, the furnace was cleaned, closed and vacuumed up to 1–10 Pa, then nitrogen was filled to protect iridium curable from oxidation during crystal growth. Then the material is heated by intermediate frequency induction supply. After the material is completely melted, the seed crystal is dipped into melt slowly when the melt surface center temperature was adjusted to the melt point of $GdScO_3$ melt, then pulled up with pull rate of 0.2–0.8 mm/h and rotating rate of 5–10 rpm. Crystal growth control software is CZControl XE, developed by Anhui Institute of Optics and Fine Mechanics of CAS, were used to grow it. The obtained boule diameter and length of Yb:$GdScO_3$ crystal are 30 mm and 37 mm, respectively, as shown in Fig. 1.

2.2. Sample performance characterization

A crystal disk was cut from the as-grown crystal and ground into powder for powder x-ray diffraction (XRD) measurement. The powder XRD measurement was carried out at room temperature with the X'pert Pro XRD of Philips company in the Netherlands. The x-ray was Cu K_α radiation, the tube voltage and current were 40 kV and 40 mA, respectively. The scanning mode was continuous scanning mode with scanning step of 0.033°, and scanning range of 10°–90°. In order to obtain good-resolution emission spectra to determine crystal field splitting, the emission spectra of the crystal were measured under the excitation of 940 nm LD by Edinburgh FLSP-920 spectrometer at temperature 8 K. The absorption spectrum of Yb:$GdScO_3$ crystal was measured by PE Lambda 950 spectrophotometer in the range of 250–3000 nm at temperature of 8 K.

3. Results and discussion

3.1. Structural characterization

The as-grown Yb:$GdScO_3$ crystal is shown in Fig. 1. It is light yellow and smooth on its surface. The whole crystal is transparent and crack-free.

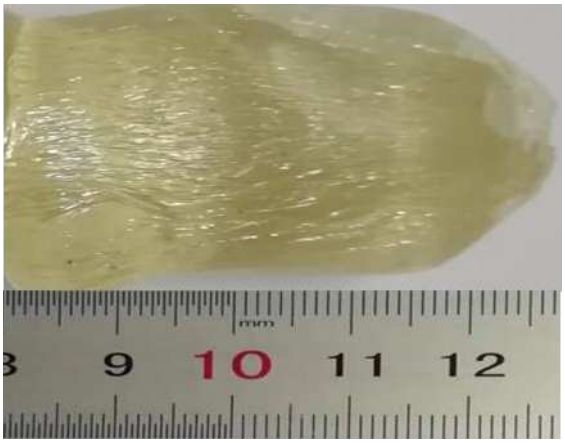


Fig. 1. Photograph of the as-grown $GdScO_3$ single crystal.

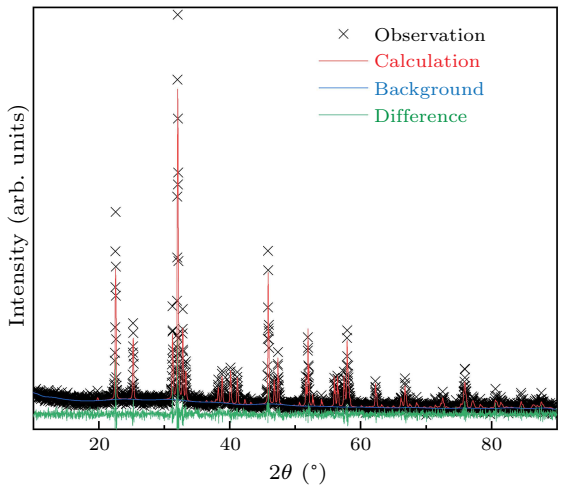


Fig. 2. Rietveld refinement results of the Yb:$GdScO_3$ crystal obtained from the XRD data, with the difference between observed data and calculated data.

The powder x-ray diffraction of Yb:$GdScO_3$ is shown in Fig. 2. Because of the same chemical valence and sim-

ilar ion radius (the radius of Yb^{3+} is 0.0985 nm, Gd^{3+} is 0.1053 nm, and the coordination number of Gd^{3+}/Yb^{3+} is 8), Gd^{3+} is easily replaced by Yb^{3+}. Rietveld refinement was performed to its XRD with software package GSAS. The lattice parameters, atomic coordinates, and temperature factors of Yb^{3+}:$GdScO_3$ were refined. The refined residuals R_P and R_{WP} are 3.48% and 4.71%, respectively, which means that the calculated results are in good agreement with the experimental data. The fitted results are shown in Fig. 2, and the structural parameters are listed in Table 1. The cell parameters are fitted to be $a = 0.5734355$ nm, $b = 0.7912412$ nm, $c = 0.5467406$ nm, and $\alpha = \beta = \gamma = 90°$. The cell volume is $V = 0.248052180$ nm^3 and the calculated crystal density is $\rho = 6.701$ g·cm^{-3}. The unit cell parameters of $GdScO_3$ are $a = 0.5750224$ nm, $b = 0.7936361$ nm, $c = 0.5485421$ nm, and the unit cell volume $V = 0.250331367$ nm^3. It can be seen that the parameters and cell volume of Yb:$GdScO_3$ decrease slightly.

Table 1. Structural parameters from the Rietveld refinement of Yb:$GdScO_3$.

Atom	Multiplicity Wyckoff letter	x	y	z	Occupancy	U_{iso}
O1	4*c*	0.482677	0.250000	0.074549	1.1586	0.01713
Sc1	4*b*	0.000000	0.000000	0.500000	1.0121	0.02462
O2	8*d*	0.160949	0.552658	0.182700	0.9975	0.02136
Gd1	4*c*	0.438608	0.750000	0.482152	0.9468	0.02548
Yb1	4*c*	0.440948	0.750000	0.469675	0.0412	0.01989
Lattice parameters	$a = 0.5734355$ nm, $b = 0.7912412$ nm, $c = 0.5467406$ nm, $\rho = 6.701$ g·cm^{-3}, $V = 0.248052180$ nm^3					
	Space group: *Pnma* (No. 62). *R* factors $R_p = 3.48\%$, $R_{wp} = 4.71\%$					

3.2. Fluorescence spectrum and crystal field energy splitting

In order to describe crystal field splitting of Yb^{3+} in $GdScO_3$, the crystal field energy levels split from term $^2F_{5/2}$ are labeled as $^2F_{5/2}(1)$, $^2F_{5/2}(2)$ and $^2F_{5/2}(3)$, from term $^2F_{7/2}$ are labeled as $^2F_{7/2}(1)$, $^2F_{7/2}(2)$, $^2F_{7/2}(3)$ and $^2F_{7/2}(4)$ from the low to high energy, respectively.

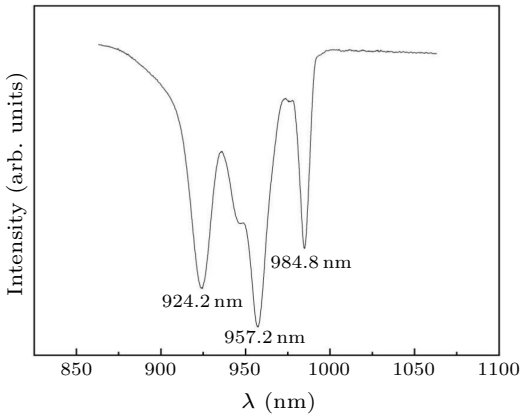


Fig. 3. Absorption spectrum of Yb:$GdScO_3$ at 8 K.

The absorption spectrum of Yb^{3+}:$GdScO_3$ at 8 K is shown in Fig. 3. Three absorption peaks at 924.2 nm, 957.2 nm and 984.8 nm are corresponding to the transitions $^2F_{7/2}(1)\rightarrow{}^2F_{5/2}(1)$, $^2F_{7/2}(1)\rightarrow{}^2F_{5/2}(2)$ and $^2F_{7/2}(1)\rightarrow{}^2F_{5/2}(3)$ respectively. Therefore, the corresponding energy levels of $^2F_{5/2}(3)$, $^2F_{5/2}(2)$ and $^2F_{5/2}(1)$ are 10820 cm^{-1}, 10447 cm^{-1} and 10154 cm^{-1}, respectively.

The emission spectrum of Yb^{3+}:$GdScO_3$ excited by 940 nm at 8 K is shown in Fig. 4. It can be observed that there exists a strong emission peak at 997.7 nm. The emission spectrum can be fitted by eleven Lorentz peaks, which are 968.7 nm, 988.1 nm, 993.0 nm, 994.7 nm, 997.7 nm, 992.2 nm, 1004.7 nm, 1009.4 nm, 1026.8 nm, 1033.6 nm, and 1058.8 nm, respectively. The emission peaks at 986.7 nm, 997.7 nm, 1026.8 nm and 1058.8 nm are corresponding to the transition energies of 10135 cm^{-1}, 10023.1 cm^{-1}, 9739 cm^{-1}, and 9445 cm^{-1}, respectively. Because the energy gaps among crystal field energy levels split from $^2F_{5/2}$ are very small (less than or nearly equal to the phonon energy), the photoluminescence transition from $^2F_{5/2}(3)$ and $^2F_{5/2}(2)$ cannot be observed due to rapid phonon relaxation process to the lowest crystal field split energy $^2F_{5/2}(1)$. The sharp peak at 997.7 nm should be assigned to the transition between the lowest crystal field energy level $^2F_{5/2}(1)$ and $^2F_{7/2}(2)$. The transition energy of 997.7 nm is 10023.1 cm^{-1}, so the energy level position of $^2F_{7/2}(2)$ should be 131 cm^{-1}. The emission peaks at 1026.8 nm and 1058.8 nm, whose transition energies are 9739 cm^{-1} and 9444.7 cm^{-1}, should be attributed to the higher and highest crystal field levels of $^2F_{7/2}$, which are labeled as $^2F_{7/2}(3)$ and $^2F_{7/2}(4)$, and their energy position can be determined to be 415 cm^{-1} and 710 cm^{-1}, respectively.

In a word, the crystal energy splittings of Yb^{3+}:$GdScO_3$ are 10154 cm^{-1}, 10447 cm^{-1}, 10820 cm^{-1} for $^2F_{5/2}$, and 0 cm^{-1}, 131 cm^{-1}, 415 cm^{-1}, 710 cm^{-1} for $^2F_{7/2}$. The energy level splitting of Yb^{3+}:$GdScO_3$ is shown in Fig. 5. The energy level splitting is slightly smaller than that of Yb:YAG ($^2F_{5/2}$: 10930 cm^{-1}, 10624 cm^{-1}, 10327 cm^{-1}; $^2F_{7/2}$: 0 cm^{-1}, 564 cm^{-1}, 606 cm^{-1}, 787 cm^{-1}).[46]

The crystal field energy level structure of $^2F_{7/2}$ can affect the population inversion property greatly. It is helpful to compare it with Yb:YAG. The crystal energy splittings of $^2F_{7/2}$ in Yb:YAG are 0 cm^{-1}, 564 cm^{-1}, 606 cm^{-1} and 787 cm^{-1}. It can be seen that the energies of $^2F_{7/2}(2)$, $^2F_{7/2}(3)$, $^2F_{7/2}(4)$ are

much higher than those of $^2F_{7/2}(1)$, which means that it is easier to realize the population inversion of $^2F_{5/2}(1)\rightarrow{}^2F_{7/2}(2)$, $^2F_{7/2}(3)$ and $^2F_{7/2}(4)$ during laser operation. For Yb:$GdScO_3$, $^2F_{7/2}(2)$ and $^2F_{7/2}(3)$ are closer to the ground state $^2F_{7/2}(1)$, so it is difficult to realize population inversion, and it is more easier to realize the laser operation from $^2F_{5/2}(1)\rightarrow{}^2F_{7/2}(4)$ with wavelength around 1060 nm.

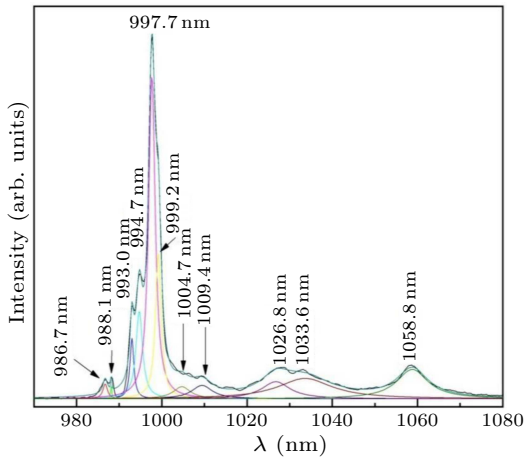


Fig. 4. Emission spectrum of Yb:$GdScO_3$ excited by laser diode of 940 nm.

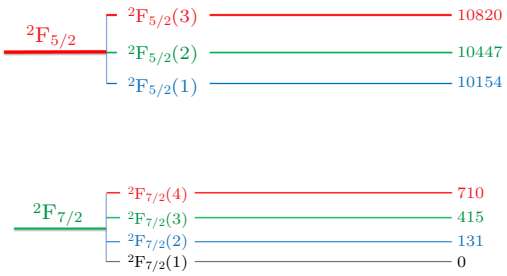


Fig. 5. Energy level splitting in cm^{-1} of Yb^{3+}:$GdScO_3$.

3.3. Determination of Hamiltonian parameters of Yb

The crystal field at a magnetic ion can be expressed as a simple sum of separate contributions from each of the ligand ions by superposition mode,[47] and crystal field parameter B_q^k calculated by intrinsic crystal field parameter $\bar{B}_k(R_0)$, ligand factor $g_{k,q}(\theta_L, \phi_L)$, and power t_k (usually t_k is taken as $k+1$),

$$B_q^k = \sum_L \bar{B}_k(R_0) g_{k,q}(\theta_L, \phi_L) \left(\frac{R_0}{R_L}\right)^{t_k}, \tag{2}$$

where R_0 is the shortest distance between the magnetic ion and all of ligands, R_L represents the distance of the L-th ligand, θ_L and ϕ_L are the angular position of the L-th ligand.[47]

The electronic configuration of Yb^{3+} is f^{13}, and its conjugate state is f^1. The Hamiltonian in $GdScO_3$ can be expressed as

$$H = E_{\rm av} + \sum_i \boldsymbol{s}_i \cdot \boldsymbol{l}_i + \sum_{k,q} B_q^k C_q^k, \tag{3}$$

where $E_{\rm av}$ is the kinetic energy of f electrons and the Coulomb interaction between them and the electrons in the nucleus and full shell, and the second term stands for spin–orbit coupling, $\boldsymbol{s}_i$ and $\boldsymbol{l}_i$ are spin and angular momentum operators of i-th f electron, ζ is the spin–orbit coupling parameter. The third term stands for the crystal field interaction, B_q^k is the crystal field parameter, and C_q^k is the angular partial operator of the crystal field. The site symmetry is mirror symmetry m or C_s normal to the orientation [010], a transformation operation $\boldsymbol{M}$ is applied on $\boldsymbol{X} = (x, y, z)^{\rm T}$ to get $\boldsymbol{X}' = (x', y', z')^{\rm T}$ so that the normal orientation of mirror symmetry is [001],

$$\begin{pmatrix} x \\ y \\ z \end{pmatrix} = \boldsymbol{M} \begin{pmatrix} x' \\ y' \\ z' \end{pmatrix}, \quad \boldsymbol{M} = \begin{bmatrix} 0 & 0 & 1 \\ 1 & 0 & 0 \\ 0 & 1 & 0 \end{bmatrix}. \tag{4}$$

The origin of $\boldsymbol{X}$ and $\boldsymbol{X}'$ is the site of Gd/Yb.

For C_s symmetry of Yb^{3+} replacing Gd^{3+} in $GdScO_3$, the (k, q) values of non-vanished B_q^k can be taken as (2, ±2), (2, 0), (4, ±4), (4, ±2), (4, 0), (6, ±6), (6, ±4), (6, ±2), and (6, 0). Three B_0^k values are real, six $B_0^k (q \neq 0)$ values are complex with 12 real variables, and there are 15 independent crystal field parameters totally.

In order to obtain the Hamiltonian parameters, firstly, the Hamiltonian matrix elements of Yb^{3+} in $GdScO_3$ were calculated in the space spanned by the base vectors $|f^{13}SLJM\rangle$ of Yb^{3+}, where $S = 1/2$, $L = 3$, $J = 7/2$ and 5/2; $M = \pm 7/2$, $\pm 5/2$, $\pm 3/2$, $\pm 3/2$ when $J = 7/2$; $M = \pm 5/2$, $\pm 3/2$, $\pm 3/2$ when $J = 5/2$. Secondly, three intrinsic crystal field parameters $\bar{B}_k$ ($k = 2, 4, 6$) were fitted to the energy levels obtained from absorption and emission transitions. Thirdly, the initial crystal filed parameters B_q^k were calculated from the intrinsic $\bar{B}_k$ obtained in step 2 and coordination factors, and would be used as initial values to fit the experimental energy levels,[46–49] in which the energy derivative is calculated by[46–49]

$$\frac{\partial \boldsymbol{E}}{\partial P_i} = \frac{\mathrm{D}[\sum_{j\neq i} P_j \boldsymbol{O}_j + (P_i + \varepsilon)\boldsymbol{O}_i] - \mathrm{D}[\sum_{j\neq i} P_j \boldsymbol{O}_j + (P_i - \varepsilon)\boldsymbol{O}_i]}{2\varepsilon}, \tag{5}$$

where P_i is the i-th Hamiltonian parameter, and $\boldsymbol{O}_i$ is the matrix corresponding to the i-th Hamiltonian parameter, D stands for the matrix diagonalization to obtain eigenvalue; ε is a very small quantity. The final step of D operation is to rearrange eigenvalues from the lowest priority to the highest.

The fitting parameters of the superposition model include $E_{\rm av}$, ζ, $\bar{B}_2$, $\bar{B}_4$, and $\bar{B}_6$, whose initial values are 0 cm^{-1}, 2900 cm^{-1}, 200 cm^{-1}, 200 cm^{-1}, and 200 cm^{-1}, respectively. If the principal of m symmetry is [010], all of B_q^k computed from coordination factor $g_{k,q}$ are real, and only B_0^k will be real and $B_q^k (q \neq 0)$ will be complex if the site symmetry principal axis is in the direction of [001]. The fitting error is smaller when the principal axis is [010], so the intrinsic crystal parameters were fitted under the principal axis [010] of C_s symmetry. The fitting results are insensitive to the initial values

of $\bar{B}_2$, $\bar{B}_4$ and $\bar{B}_6$, which indicates that the fitting is reasonable. The orthogonal coordinates of coordination oxygen are shown in Table 2, which is used to calculate coordination factor $g_{k,q}$. After 19 iterations, the root-mean-square deviation σ is 27 cm^{-1} [$\sigma = \sqrt{\sum_i (E_{\mathrm{exp},i} - E_{\mathrm{cal},i})^2/N}$], where $E_{\mathrm{exp},i}$ and $E_{\mathrm{cal},i}$ stand for the i-th experimental and calculated energy levels, N is total number of fitted energy levels, and the relative residual factor R is 0.31%. The obtained Hamiltonian parameters E_{av}, ζ, $\bar{B}_2$, $\bar{B}_4$, and $\bar{B}_6$ are 4668, 2899, −4812, 3681, and −637 in cm^{-1}, respectively. The crystal field parameters B_q^k computed from $\bar{B}_k$ and coordination factor $g_{k,q}$ with principal axis [010] and [001] are listed in Table 4. B_q^k with symmetry axis [001] were used as the initial parameters for further energy level fitting, where E_{av}, ζ and B_q^k are variable. After 16 iterations, the root-mean-square deviation σ is 9 cm^{-1}, the relative residual factor R is 0.6%. The calculated and experimental energy levels are consistent very well with each other, and the final crystal filed parameters are listed in Table 3.

It can be seen that B_0^6 changes from −87 cm^{-1} to 155 cm^{-1}, B_4^4 from $(26+232\mathrm{I})$ cm^{-1} to $(-5+455)$ cm^{-1}, B_2^6 from $(45-29\mathrm{I})$ cm^{-1} to $(-42-114\mathrm{I})$ cm^{-1}, the signs of the other B_q^k are the same as those computed from $\bar{B}_k$. Based on this case, the real parameters B_q^k computed with $\bar{B}_k$ of symmetry axis [010] were used to analyzed further, among which, except B_0^2, B_2^4 and B_4^6 with positive values, the other B_q^k are negative and the absolute maximal value is 1566 cm^{-1}, which indicates that the ligand point charge, covalency and overlap interaction are slightly weaker than charge interpenetration and Coulomb exchange. The B_q^k values of Yb:YAG have also been listed in Table 4, only B_0^2, B_6^6 and B_2^6 are negative among nine crystal field parameters, the others are positive, indicating that the ligand point charge, covalency and overlap interaction are important in YAG.

Table 2. The ligand coordinate data of Gd/Yb in $GdScO_3$.

AtomGd/Yb	(x, y, z) in Å	(x', y', z') in Å
Gd/Yb	0,0,0	0,0,0
O1O	−0.7821, 2.4753, 1.1447	1.1447, −0.7821, 2.4753
O2	−1.4069, 1.4877, −1.5963	1.5963, −1.4069, 1.4877
O3	1.4641, 1.4877, −0.9681	−0.9681, 1.4641, 1.4877
O4	1.4641, −1.4877, −0.9681	−0.9681, 1.4641, −1.4877
O5	1.4069, −1.4877, −1.5963	−1.5963, −1.4069, −1.4877
O6	0.7821, −2.4753, 1.1447	1.1447, −0.7821, −2.4753
O7	0.6315, 0, 2.1709	2.1709, 0.6315, 0
O8	−2.2395, 0, 0.7467	0.7467, −2.2395, 0

Table 3. The experimental, calculated energy levels E_{exp}, E_{cal} and their difference (Δ) of Yb:$GdScO_3$.

Yb:$GdScO_3$/cm^{-1}				
E_{exp}	E_{cal} (SM)	Δ (SM)	E_{cal} (CFP)	Δ (CFP)
0	−25	25	−1	1
131	125	6	132	−1
415	440	−25	418	−3
710	715	−5	716	−6
10154	10189	−37	10156	−2
10447	10428	19	10444	3
10820	10803	17	10813	7
	$R = 0.31\%$	$\sigma = 21$ cm^{-1}	$R = 0.06\%$	$\sigma = 4$ cm^{-1}

Table 4. The crystal field parameters of Yb:$GdScO_3$ and Yb:YAG.[46]

	Yb:$GdScO_3$			Yb:YAG	
k,q	B_q^k/cm^{-1} (SM) with symmetry axis [010]	B_q^k/cm^{-1} (SM) with symmetry axis [001]	B_q^k/cm^{-1} (CFP) with symmetry axis [001]	B_q^k/cm^{-1} (SM)	B_q^k/cm^{-1} (CFP)
2,2	−307	$-11-43\mathrm{I}$	$-223-527\mathrm{I}$	244	269
2,0	191	−12	−896	−200	585
4,4	−1566	$26+232\mathrm{I}$	$-5+455\mathrm{I}$	180	−740
4,2	122	$-52-134\mathrm{I}$	$-34-136\mathrm{I}$	575	285
4,0	−372	−91	−183	1028	1585
6,6	−206	$-35+20\mathrm{I}$	$-73+31\mathrm{I}$	−1436	−44
6,4	416	$-218+3\mathrm{I}$	$-18+47\mathrm{I}$	9.4	677
6,2	−206	$45-29\mathrm{I}$	$-42-114\mathrm{I}$	−968	−67
6,0	−773	−87	155	1507	1387

4. Conclusion and perspectives

In this work, (5 at.%)Yb:$GdScO_3$ single crystal is grown by the Czochralski method, its structure parameters are fitted to XRD by Rietveld refinement, the unit cell parameters and atomic coordinates are obtained. Its crystal filed energy level splitting of Yb:$GdScO_3$ is determined by the absorption and photoluminescence spectra at 8 K. Among its crystal field energy levels from $^2F_{7/2}$, only $^2F_{7/2}(4)$ is far from the ground state $^2F_{7/2}(1)$ by 710 cm^{-1}, so it is more easier to realize the laser operation of $^2F_{5/2}(1)\rightarrow{}^2F_{7/2}(4)$. The spin–orbital coupling parameters, intrinsic crystal field parameters, and crystal field parameters of Yb:$GdScO_3$ are fitted to its crystal field energy splitting. B_q^k of the symmetry principal [010] indicates that the ligand point charge, covalency and overlap interaction are slightly weaker than charge interpenetration and coulomb exchange for Yb^{3+} in $GdScO_3$, which is in contrary to Yb:YAG.

Acknowledgments

This work was supported by the National Key Research and Development Program of China (Grant

Nos. 2022YFB3605700 and 2023YFB3507403), the National Natural Science Foundation of China (Grant No. 52272011), the Youth Innovation Promotion Association of CAS (Grant No. 2023463), Plan for Anhui Major Provincial Science & Technology Project (Grant No. 202203a05020002), and Open Project of Advanced Laser Technology Laboratory of Anhui Province (Grant No. AHL20220ZR04).

References

[1] Wang D, Hou W, Li N, Xue Y, Wang Q, Xu X, Li D, Zhao H and Xu J 2019 *Opt. Mater. Express* **9** 4218
[2] Schäfer A, Besmehn A, Luysberg M, Winden A, Stoica T, Schnee M, Zander W, Niu G, Schroeder T, Mantl S, Hardtdegen H, Mikulics M and Schubert J 2014 *Semicond Sci. Technol.* **29** 075005
[3] Rumyantsev S, Stillman W, Shur M, Heeg T, Schlom D G, Koveshnikov S, Kambhampati R, Tokranov V and Oktyabrsky S 2012 *Int. J. High Speed Electron. Syst.* **20** 105
[4] Sheng J M, Kan X C, Ge H, Yuan P Q, Zhang L, Zhao N, Song Z M, Yao Y Y, Tang J N, Wang S M, Tian M L, Tong X and Wu L S 2020 *Chin. Phys. B* **29** 057053
[5] Lin S H, Lin Z Q and Chen C W 2021 *Ceram. Int.* **47** 16828
[6] Schäfer A, Rahmanizadeh K, Bihlmayer G, Luysberg M, Wendt F, Besmehn A, Fox A, Schnee M, Niu G, Schroeder T, Mantl S, Hardtdegen H, Mikulics M and Schubert J 2015 *J. Alloys Compd.* **651** 514
[7] Uecker R, Velickov B, Klimm D, Bertram R, Bernhagen M, Rabe M, Albrecht M, Fornari R and Schlom D G 2008 *J. Cryst. Growth* **310** 2649
[8] Chaix-Pluchery O and Kreisel J 2009 *J. Phys.: Condens. Matter.* **21** 175901
[9] Mansley Z R, Mizzi C A, Koirala P, Wen J and Marks L D 2020 *Phys. Rev. Mater.* **4** 045003
[10] Grover V, Shukla R, Jain D, Deshpande S K, Arya A, Pillai C G S and Tyagi A K 2012 *Chem. Mater.* **24** 2186
[11] Li Q, Dong J, Wang Q, Xue Y, Tang H, Xu X and Xu J 2020 *Opt. Mater.* **109** 110298
[12] Aamir M, Bibi I and Ata S 2021 *Ceram. Int.* **47** 16696
[13] Jia J H, Ke Y J, Zhang X X, Wang J F, Su L, Wu Y D and Xia Z C 2019 *J. Alloys Compd.* **803** 992
[14] Wu Y D, Chen H, Hua J Y, Qin Y L, Ma X H, Wei Y Y and Zi Z F 2019 *Ceram. Int.* **45** 13094
[15] Chopelas A 2011 *Phys. Chem. Miner.* **38** 709
[16] P N R S, Panda D P and Sundaresan A 2021 *J. Phys. Chem. C* **125** 10803
[17] Hidde J, Guguschev C, Ganschow S and Klimm D 2018 *J. Alloys Compd.* **738** 415
[18] Chaix-Pluchery O and Kreisel J 2011 *Phase Transit.* **84** 542
[19] Veličkov B, Kahlenberg V, Bertram R and Bernhagen M 2007 *Z. für Kristallogr.* **222** 466
[20] Mizzi C A, Koirala P and Marks L D 2018 *Phys. Rev. Mater.* **2** 025001
[21] Levy M 2004 *Solid State Ion.* **175** 349
[22] Peng F, Liu W, Zhang Q, Luo J, Sun D, Sun G, Zhang D and Wang X 2018 *J. Lumin.* **201** 176
[23] Ruffo A, Mozzati M C, Albini B, Galinetto P and Bini M 2020 *J. Mater. Sci.: Mater. Electron.* **31** 18263
[24] Paull R J, Mansley Z R, Ly T, Marks L D and Poeppelmeier K R 2018 *Inorg. Chem.* **57** 4104
[25] Chaix-Pluchery O, Sauer D and Kreisel J 2010 *J. Phys.: Condens. Matter.* **22** 165901
[26] Peng F, Liu W, Luo J, Sun D, Chen Y, Zhang H, Ding S and Zhang Q 2018 *Crystengcomm* **20** 6291
[27] Gupta S K, Grover V and Shukla R 2016 *Chem. Eng. J* **283** 114
[28] Li S, Fang Q, Zhang Y, Tao S, Zhang J, Quan C, Sun D, Zhao C and Hang Y 2021 *Opt. Laser Technol.* **143** 107345
[29] Hu D, Dong J, Tian J, Wang W, Wang Q, Xue Y, Xu X and Xu J 2021 *J. Lumin.* **238** 118243
[30] Li Q, Dong J, Wang Q, Zhao H, Xue Y, Tang H, Xu X and Xu J 2021 *J. Lumin.* **230** 117681
[31] Hou W, Zhao H, Qin Z, Liu J, Wang D, Xue Y, Wang Q, Xie G, Xu X and Xu J 2020 *Opt. Mater. Express* **10** 2730
[32] Liu Z, Toci G, Pirri A, Patrizi B, Feng Y, Wei J, Wu F, Yang Z, Vannini M and Li J 2020 *J. Adv. Ceram.* **9** 674
[33] Ma J, Yang F, Gao W, Xiaodong X, Jun X, Shen D and Tang D 2021 *Opt. Lett.* **46** 2328
[34] lvarez-Pérez J O, Cano-Torres J M, Ruiz A, Serrano M D, Cascales C and Zaldo C 2021 *J. Mater. Chem. C* **9** 4628
[35] Soharab M, Bhaumik I, Bhatt R, Saxena A, Khan S, Goutam U K and Karnal A K 2021 *J. Lumin.* **231** 117736
[36] Wang W, Jiang B, Feng T, Fan J, Ma W, Guo W, Li J and Zhang L 2021 *J. Am. Ceram. Soc.* **104** 6064
[37] Zhao Y, Wang Q, Meng L, Yao Y, Liu S, Cui N, Su L, Zheng L, Zhang H and Zhang Y 2021 *Chin. Opt. Lett.* **19** 041405
[38] Petrov V A, Petrov V V, Kuptsov G V, Laptev A V, Galutskiy V V and Stroganova E V 2021 *Laser Phys.* **31** 035003
[39] Chen J, Dong L, Liu F, Xu H and Liu J 2021 *Crystengcomm* **23** 427
[40] Demirbas U, Kellert M, Thesinga J, Hua Y, Reuter S, Krtner F X and Pergament M 2021 *Appl. Phys. B* **127** 46
[41] Basyrova L, Loiko P, Maksimov R, Shitov V, Serres J M, Griebner U, Petrov V, Aguiló M, Díaz F and Mateos X 2021 *Ceram. Int.* **47** 6633
[42] Volokitina A, David S P, Loiko P, Subbotin K, Titov A, Lis D, Solé R M, Jambunathan V, Lucianetti A, Mocek T, Camy P, Chen W, Griebner U, Petrov V, Aguiló M, Díaz F and Mateos X 2021 *J. Lumin.* **231** 117811
[43] Stephen S K and Varghese T 2021 *Mater. Charact.* **174** 110985
[44] Wang A, Zhang J, Ye S, Ma X, Wu B, Wang S, Wang F, Wang T, Zhang B and Jia Z 2021 *Crystals* **11** 78
[45] Zhang Y, Li S, Du X, Guo J, Gong Q, Tao S, Zhang P, Fang Q, Pan S, Zhao C, Liang X and Hang Y 2021 *Opt. Lett.* **46** 3641
[46] Wang X M, Wang X F and Zhang Q L 2015 *J. Synth. Cryst.* **44** 1465
[47] Newman D J 2007 *Crystal Field Handbook* 2nd Edn. (New York: Cambridge University Press) p. 83
[48] Zhang Q L, Ning K J, Ding L H, Liu W P, Zhou W L, Jiang H H and Yin S T 2010 *Chin. Phys. B* **19** 087501
[49] Zhang Q L, Ning K J, Ding L H, Liu W P, Sun D L, Jiang H H and Yin S T 2013 *Chin. Phys. B* **22** 067105